Finite element analysis of the plastic deformation zone and working load in equal channel angular extrusion

S. Li [a,*], M.A.M. Bourke [a], I.J. Beyerlein [b], D.J. Alexander [a], B. Clausen [c]

[a] *Materials Science and Technology Division, Los Alamos National Laboratory, Los Alamos, NM 87545, USA*
[b] *Theoretical Division, Los Alamos National Laboratory, Los Alamos, NM 87545, USA*
[c] *Neutron Science Center, Los Alamos National Laboratory, Los Alamos, NM 87545, USA*

Abstract

A comprehensive finite element (FE) study is conducted to analyze the formation of the plastic deformation zone (PDZ) and evolution of the working load with ram displacement during a single pass of equal channel angular extrusion (ECAE) with intersection angle 90°. This study explores systematically the coupled effects of material response, outer corner angle ($\Psi = 0°$, 45°, or 90°), and friction on ECAE deformation, which can be effectively analyzed through two key characteristics of the PDZ alone. These characteristics, the morphology and strain-rate distribution within the PDZ, are largely responsible for the heterogeneity in strain that develops in the sample at the end of a single pass. Strain hardening, Ψ, and friction were all found to have some effect on the PDZ, though under their combined influence, one tends to dominate over the others. Strain hardening tends to produce asymmetry in the strain-rate distribution within the PDZ, resulting in corner gaps and a more heterogeneous strain distribution than an ideal perfectly plastic material. In cases in which the material fills the die, the PDZ shape is largely governed by the die geometry, i.e. Ψ, independent of material response and friction. In this respect, friction does however help to reduce the free surface gaps that form between a strain hardening material and the die, but to further increase the degree of heterogeneity. The distinct stages that are present in the load versus displacement curves are defined and associated with those in sample deformation, some of which depend on Ψ and others on material properties. Effective strain calculations are compared with various analytical models and the one that directly accounts for the PDZ tends to perform better. To date, most of the cases studied here have not been modeled analytically; however, a stronger connection between analytical modeling and actual ECAE deformation can be made by the guidance of these FE studies on the interactive influence of processing and material variables.
Published by Elsevier B.V.

Keywords: Equal channel angular extrusion; Finite element; Plastic deformation zone; Severe plastic deformation

1. Introduction

One of the main processing techniques for introducing severe plastic deformation, equal channel angular extrusion (ECAE) can be utilized to produce materials with ultra-fine size grains in bulk [1]. In ECAE, a billet is pressed through a die that contains two equal cross-sectional channels meeting at an angle Φ, and the outer corner meeting at an angle Ψ (see Fig. 1a). Because the cross-section of the billet remains the same during extrusion, the process can be repeated until the accumulated deformation reaches a desired level. The process, however, is not monotonic as re-inserting the

billet leads to a change in the strain path from pass to pass. Therefore multi-pass extrusions with a variable sequence of strain path change can deform a sample in a complex manner. Under such conditions, submicron microstructures can potentially evolve which offer remarkable mechanical and physical properties, such as ultra-high strength and ductility [2,3]. Each time the billet is extruded, it undergoes intense plasticity, within a region in the intersection corner of the two channels, denoted as the plastic deformation zone (PDZ). The evolution and uniformity in microstructure and in turn, material properties, will depend on the characteristics of the PDZ. A sound knowledge of the PDZ is necessary in understanding the process–structure–property relationships and in optimization of tool designs and processing variables.

Analytical studies have been carried out to investigate the deformation behavior of the billet during ECAE, such as

---

* Corresponding author. Tel.: +1 505 665 6054; fax: +1 505 665 2676.
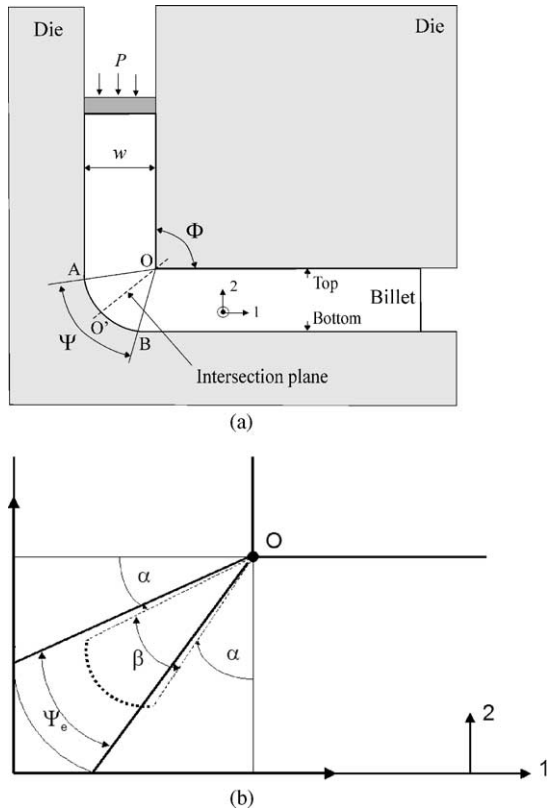*E-mail address:* saiyi@lanl.gov (S. Li).

Fig. 1. (a) ECAE die geometry featuring the die angle Φ and outer corner angle Ψ. The die fan AOB, the intersection plane (OO′), the width w of the channels, and the top and bottom surfaces of the billet are indicated. (b) The definition of α and β angles associated with the plastic deformation zone (see Eq. (3)) and the angle Ψ_e, associated with the size of the free surface corner gap.

strain analyses based on slip line theory and geometric considerations [2,4–7] or stress analyses based on upper bound theory [8]. Some of the earliest considered simple shear deformation and used geometric analyses to determine a scalar measure of strain. Segal [2] derived an analytical expression to estimate the shear strain for the case of die angle Φ and a sharp outer corner ($\Psi = 0°$), which corresponds to concentrated simple shear along the intersection plane. The von Mises equivalent strain in this case is

$$\varepsilon = \frac{2\cot(\Phi/2)}{\sqrt{3}} \qquad (1)$$

Later, a modified form was proposed by Iwahashi et al. [6] to consider a die with a rounded outer corner ($\Psi > 0°$). According to their model, the effective strain per pass can be calculated from Φ and Ψ by

$$\varepsilon = \frac{1}{\sqrt{3}}\left[2\cot\left(\frac{\Phi}{2} + \frac{\Psi}{2}\right) + \Psi \csc\left(\frac{\Phi}{2} + \frac{\Psi}{2}\right)\right] \qquad (2)$$

Common assumptions in these geometric analyses include: die surfaces are frictionless, the plastic flow occurs uniformly on a plane, the billet completely fills the die channel, and the material behavior is close to ideal (rigid perfectly

plastic). Thus the implications of an extended PDZ are not explicitly considered. There are a few analyses that consider directly the shape of the PDZ [5,9] but they apply to idealized conditions of perfectly plastic behavior. For instance, using slip line theory, Segal [5] estimated the extent of PDZs for sharp and round corner dies as a result of uniform friction. According to his model, for sharp corner dies, $\Psi = 0°$, a PDZ in the shape of a fan is formed and we denote the inner angle of this PDZ as β. (Segal related β being zero for frictionless conditions and increasing with friction up to a maximum value of $\beta = \pi/2$.) In ideal rigid perfectly plastic conditions, β is centered and its two boundaries situated an angle α from the entry and exit planes of the die corner, i.e. $\beta = \pi/2 - 2\alpha$ for $\Phi = 90°$ (see Fig. 1b). In [9], the authors determined a von Mises equivalent strain associated with this PDZ, rather than the die tooling as in Eq. (2), which was found to be

$$\varepsilon = \sqrt{\frac{1}{3}}\sqrt{1 + 2a(1 - b + a) + b^2} \qquad (3)$$

where $a = \sin 2\alpha$ and $b = (1 + \beta)\tan\alpha$. ε increases from 0.5774 for $\beta = \pi/2$ to 1.1547 for $\beta = 0$. Eq. (3) applies to $\Phi = 90°$ only. The simple shear on the intersection plane ($\beta = 0$ or Eq. (1)) and distributed shearing over a central fan PDZ ($\Psi > 0$) both lead to homogeneous deformation [5,9].

ECAE deformation, however, is generally non-homogeneous (e.g. [10]), especially when the die is rounded or if conditions lead to a free surface corner gap. As observed in rounded corner dies, $\Psi > 0°$, a fan-like PDZ still develops imposing intense shearing, except near the rounded outer corner where low shear deformation evolves and the refined microstructure does not develop [10]. Similarly when material strain hardening is prevalent, a free surface corner gap forms, leading to a non-central PDZ and again, a low shear deformation in the outer corner [12]. In [9,10], the deformation and velocity gradients associated with a central fan PDZ and a bottom region of low shear deformation were determined. They showed the influence of the central fan angle β and of the low shear region on texture and microstructure development. Although these analytical analyses [5,9] surpass Eqs. (1) and (2), they do not directly account for the effect of strain hardening, much less its effect in combination with friction and/or die geometry.

To overcome these limitations, finite element (FE) analyses have been carried out. Compared to analytical approaches, the FE method accounts more realistically for the material properties and boundary conditions and can serve as a guide for analytical models. FE has been applied to investigate many factors that influence the deformation, including (i) material constitutive behavior (strain hardening or softening, strain-rate sensitivity) [11–14], (ii) die geometry (Φ, Ψ, moving die) [11,15–19], and (iii) processing variables (such as friction, backpressure, and thermal condition) [11,15,20–24]. Primary concerns were the conditions typically that lead to incomplete filling in the die and strain inhomogeneity in the deformed billets.

To date, relatively little attention has been paid to on the characteristics of the PDZ, especially as a function of material properties and friction conditions. Two chief characteristics of the PDZ are its morphology and distribution of strain-rates. Together they determine the inhomogeneity in strain distribution of the extruded billet. So for example, while the shape of the PDZ may be insensitive to a change in material response, its strain-rate distribution may not be and hence the final strain distributions for two material responses will be different.

There are a few notable studies that evaluate the deformation zone, based on FE prediction of the distribution of effective strain-rate [11,13,19]. Semiatin et al. [11] considered both strain hardening and strain-rate sensitivity using a complex die with a sliding bottom floor and $\Phi = 90°$ ($\Psi = 0°$). However, the simulations were carried out using a relatively coarse mesh, and steady-state deformation was not evident from the presented results (Fig. 7a in [11]). In another study using a die with $\Phi = 90°$ and $\Psi = 0°$, Kim et al. [13] showed that an increase in the strain hardening coefficient of the sample increases the corner gap and an increase in its strain-rate sensitivity broadens the PDZ. Kim [19] also assessed the effect of die geometry on the PDZ developed in a rigid perfectly plastic material using dies with $\Phi = 90°$ ($\Psi = 0°$, 45°, or 90°) and $\Phi = 135°$ ($\Psi = 0°$ or 45°), and found that the larger Φ or Ψ, the larger the PDZ. Frictionless conditions were assumed in both studies.

Another aspect of importance in tool designs, though rarely addressed in FE studies to date, is the working load versus ram displacement relationship. Zuyan and Zhongjin [25] evaluated the effects of various factors on the load during the so-called equal-cross-section lateral extrusion process, which appears to be equivalent to ECAE, based on FE simulations for dies with a lateral extrusion angle $15° \leq \theta \leq 60°$ (equivalent to $120° \leq \Phi \leq 165°$). However, the results are of limited value because the billet length-to-diameter ratios used, ranging from 1 to 3, mostly 1.5, were too short to achieve steady state. Furthermore, their simulations considered an initial clearance (gap) between the billet and the die wall, which might result in significant compressive deformation along the billet length at the beginning of the process. Kim [26] simulated the load–displacement curve in one-pass ECAE of an 1100 aluminum alloy using a die with $\Phi = 90°$ and $\Psi = 90°$ and explained the characteristics of the curve in five stages. In another study, Kim [27] predicted the load–displacement curve in equal channel multi-angular pressing, a die containing more than one channel intersection to simulate multiple passes in 2-D, of a pure Cu alloy using a die with $\Phi = 90°$ and $\Psi = 0°$. It was assumed in both studies that the interface between the billet and the die was frictionless. More detailed studies on the effect of important factors such as friction and material properties on the load–displacement curves are still necessary.

Systematic studies of the effect of material properties, die geometry, and friction condition on the PDZ and working load are still lacking. Collectively, the FE studies to date address a wide range of cases, including various combinations of Ψ, friction and material response. However, the studies differ from one to another in mesh density, billet length-to-channel length, billet length-to-width ratio, die angle, and how results are presented, all factors that influence the numerical results or make it difficult to compare results from study to study. Though more numerical in nature than physical, the influence of some of these factors is also explored here.

The work presented here attempts to provide a comprehensive study of the PDZ development and the evolution of working load versus displacement in one pass ECAE, with emphasis on the combined effects of material strain hardening, friction coefficient μ and Ψ. For this purpose, 2-D plane strain FE simulations were performed using dies with an intersection angle of 90°. Simulations included all possible combinations of two material types, an elastically perfectly plastic material and a elastic-strain hardening material, three different outer corner angles $\Psi = 0°$, 45°, and 90°, and for each of these, frictionless and at least one non-zero friction coefficient. The paper is organized as follows. Section 2 contains details of the FE simulations including some mesh studies. Section 3 presents under frictionless conditions the effects of strain hardening and Ψ on the PDZ, defined by yield indicators (shape) and strain-rate distribution for the frictionless case. Then, the effect of friction on PDZ development will be investigated by repeating these simulations but using the maximum applicable friction coefficient, $\mu_m > 0$. Finally, the effects of straining hardening, Ψ and friction condition on the simulated load–displacement curves will be discussed in relation to the stages in billet deformation during a single pass.

2. Finite element simulations

Simulations of a single ECAE pass assuming plane strain conditions were carried out using the FE software ABAQUS [28]. Three factors were varied in the simulations: material strain hardening, Ψ, and friction coefficient, μ. Table 1 displays a layout of the simulations performed. The stress–strain curves of the two hypothetical materials are illustrated in Fig. 2. The first material is elastic-perfectly plastic (PP) with a yield stress of 31 MPa and the second material is elastic-plastic with the same yield stress, but strain hardening (SH). Its flow stress evolves with strain according to

$$\sigma \text{ (MPa)} = 250(\bar{\varepsilon}^p)^{0.335} + 31 \tag{4}$$

where σ is the flow stress (in MPa) and $\bar{\varepsilon}^p$ denotes the equivalent plastic strain. The elastic properties of both materials were arbitrarily selected and are equivalent with a Young's modulus of 110 GPa and a Poisson's ratio of 0.35. Fig. 1a is a schematic of the die with $\Phi = 90°$ and variable outer angle Ψ. Three variants of this die with $\Psi = 0°$, 45°, or 90°, were considered. As shown in Table 1, for each combina-

Table 1
List of the FE simulations performed

Case number	Material	Outer corner angle, Ψ (°)	Friction coefficient, μ
1	Elastic-perfectly plastic (PP)	0	0
2	PP	45	0
3	PP	90	0
4	Elastic-strain hardening (SH)	0	0
5	SH	45	0
6	SH	90	0
7	PP	0	0.025 (μ_m)
8	PP	45	0.150 (μ_m)
9	PP	90	0.150 (μ_m)
10	SH	0	0.075 (μ_m)
11	SH	45	0.100 (μ_m)
12	SH	90	0.125 (μ_m)

μ_m is the maximum applicable friction for the billet length-to-width ratio 8.3 and outlet channel length-to-width ratio 4.

tion of material (PP or SH) and geometry ($\Psi = 0°$, 45°, or 90°), the simulations are first carried out assuming frictionless sliding between the billet and the tools, i.e. $\mu = 0$, and then carried out with different friction coefficients starting at $\mu = 0.025$ and increasing in increments of 0.025. In doing so, a maximum "applicable" friction coefficient μ_m, for which a simulation could be completed and a steady-state in the billet could be achieved, was determined for each case.

The FE calculations were intended to describe a die that is commonly used. The width of the billet is denoted as w (=10 mm) and the billet length was 8.3w. A fillet with radius of 0.16w was assigned to the outer side corner of the billet head to facilitate easy start of the simulations. Both the inlet and outlet channels have the same width as the billet. The length of the inlet channel is 8.8w such that the billet is fully accommodated in the channel at the start of the process. The length of the outlet channel is 4w.

The billet length-to-width ratio and the ram displacement were selected to obtain a well-defined steady-state region in the billet after one pass. The billet was inserted vertically in the inlet with the front face a distance 0.83w from the lower

horizontal face. The process simulation used a flat-faced ram to extrude the billet for a total ram displacement of 7.18w in 11.3 s. Because the total displacement was longer than the length of the outlet channel, the billet partly exits the outlet channel at the end of the simulation, allowing us to investigate bending induced by inhomogeneous deformation. For this reason, a fillet with radius of 0.1w was attached to the top and bottom ends of the outlet channel (see e.g. Fig. 3a) to avoid convergence difficulties that arise when the head of the billet exits the outlet channel. The die and the ram were treated as analytical rigid surfaces and the billet was represented using 4-node plane strain elements with linear integration.

Before performing the FE simulations, a convergence test was carried out [case 1: PP, $\Psi = 0°$, $\mu = 0$] to assess the sensitivity of the results to mesh refinement. The three meshes studied, using 10, 20, and 30 elements[1] along the width w (corresponding, respectively, to a total of 839, 3379, and 7811 elements), are shown in Fig. 3a. The corresponding equivalent plastic strain distributions along the billet width in the steady-state region are shown in Fig. 3b. The differences between the 839 mesh and the other two are significant, but between the 3379 and 7811 element meshes, they are small. Accordingly, the 3379-element mesh was adopted in all remaining simulations.

The radius at the inner corner of the die R_i is set to 0.025w. The reason for using $R_i = 0.025w$ at the inner die corner is to reduce computation time, as CPU time for the simulation with $R_i = 0$ is about 2 times that for $R_i = 0.025w$. To illustrate the effect of R_i, test simulations were carried out using $R_i = 0$ and 0.025w, for case 1 [PP, $\Psi = 0°$, $\mu = 0$]. As shown in Fig. 4, R_i mainly influences the deformation near the surface regions. Compared to $R_i = 0.025w$, $R_i = 0$ leads to slightly higher plastic deformation near the top surface of the billet and lower plastic deformation near the bottom surface.
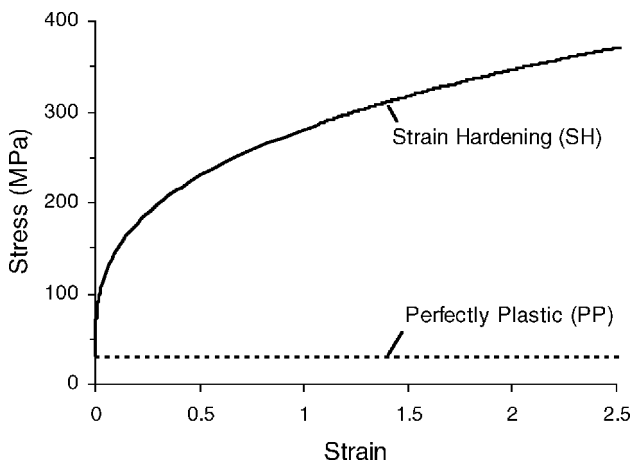

Fig. 2. Flow curves of the perfectly plastic and strain hardening material used in the FE simulations.

---

[1] There are less elements at the leading end of the billet where the fillet exists.
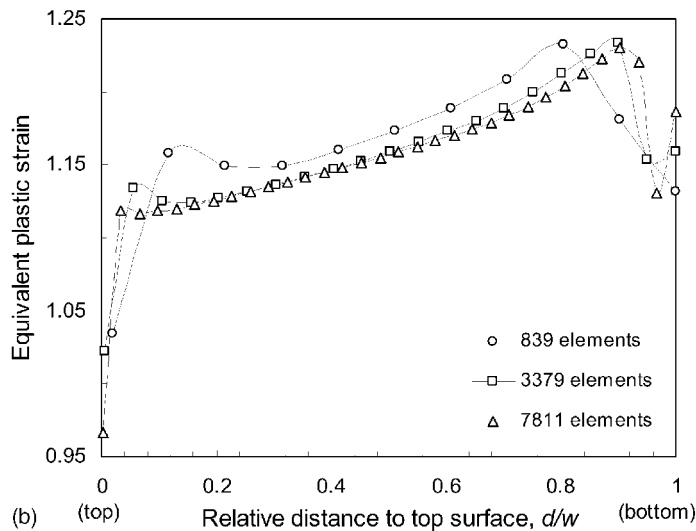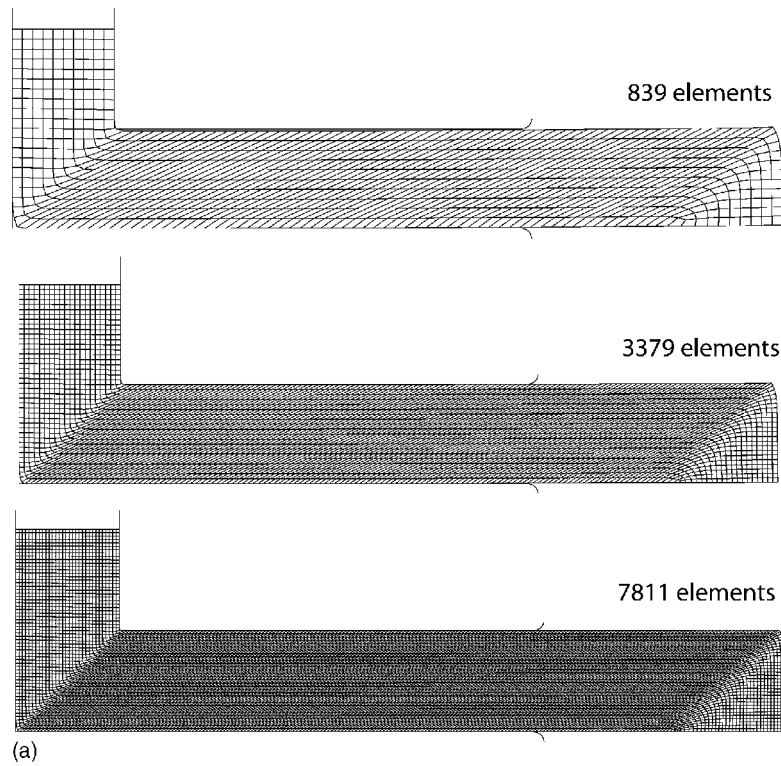
Fig. 3. The influence of mesh size (839, 3379, and 7811 elements) on (a) the deformed meshes and the (b) distribution of equivalent plastic strain along the billet width in the steady-state region. The simulations were performed for case 1 [PP, $\Psi = 0°$, $\mu = 0$].

3. Results and discussion

3.1. Deformation behavior under frictionless conditions

3.1.1. Global deformation behavior

We examine the global deformation after reaching steady state in one pass, primarily to study the ability of these materials to fill the die. Particularly under frictionless conditions, gaps can form between the material and the die at the outer corner, and the top and bottom surfaces of the exit channel. (Adding friction with all else being equal tends to decrease

the gap size.) Figs. 5 and 6 show, respectively, the deformed meshes of the billets for the PP and SH materials. The two end points of the lateral front surface of the billet prior to deformation are indicated in these figures by arrows. For the PP material (Fig. 5a), the outer corner gaps are insignificant except for a very small gap, less than one element size, for $\Psi = 0°$ and an even smaller gap where the straight outer wall of the inlet channel meets with the rounded outer corner for $\Psi = 45°$ (Fig. 5b). For this ideal PP material, these tiny corner gaps are likely caused by the discontinuity of the die wall in the FE model, rather than anything physical. The
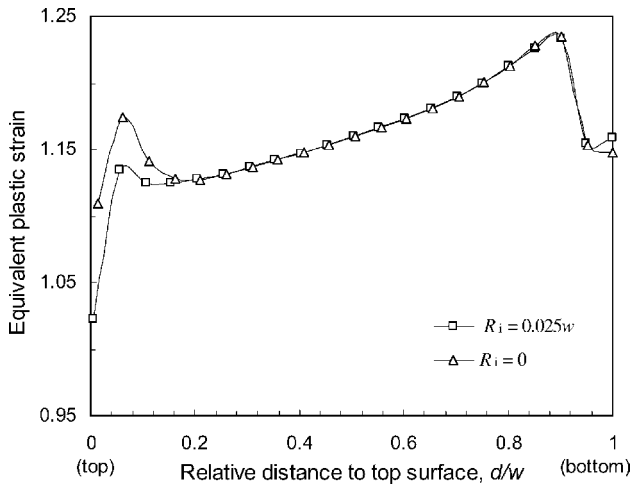
Fig. 4. Influence of inner radius ($R_i = 0$ and $0.025w$) on the distribution of equivalent plastic strain along the billet width in the steady-state region of the billets simulated for case 1 [PP, $\Psi = 0°$, $\mu = 0$].

inhomogeneous deformation generated by a nonzero Ψ has the effect of creating gaps in the outlet channel: one near the inner corner, and the other at the bottom near the end of the channel, both nonetheless associated with the slight upward bending of the billet. This upward bending and the associated gaps in the outlet channel are more evident for $\Psi = 90°$ (Fig. 5c) than $\Psi = 45°$ (Fig. 5b).

Compared to the PP material, the SH material depicts considerable differences with respect to die filling. For $\Psi = 0°$ (Fig. 6a) and $\Psi = 45°$ (Fig. 6b), actual corner gaps develop. SH results in a variation in flow stress from the inner to outer corner, which causes the material to separate from the straight inlet channel wall. However for $\Psi = 45°$ (Fig. 6b) and $\Psi = 90°$ (Fig. 6c), the SH material shows less significant upward bending and thus smaller gaps in the outlet channel as compared to the PP material.

To view these results another way, we define a material angle Ψ_e, which is the angular span of the corner gap defined where the material first separates from the inlet channel to where it rejoins the outlet channel (as indicated in Fig. 1b). In general Ψ_e is equal to Ψ when no corner gap develops (see e.g. Figs. 5c and 6c for $\Psi = 90°$) and is larger than Ψ when a corner gap forms (see Fig. 6a and b). The difference between Ψ_e and Ψ increases with the corner gap size. The values of Ψ_e measured from the deformed FE mesh at the end of these simulations are shown in Table 2. Table 2 further shows that the corner gap ($\Psi_e > \Psi$) (1) decreases with Ψ in both materials, being zero for $\Psi = 90°$ and (2) for the same Ψ is smaller in the PP material than in the SH material. This indicates that the material flow in the PP material follows the die geometry in the corner more closely than in the SH material. For dies with $\Phi = 90°$ and $\Psi = 0°$, these effects of SH on the corner gap size are consistent with the experimental observations and FE calculations made by
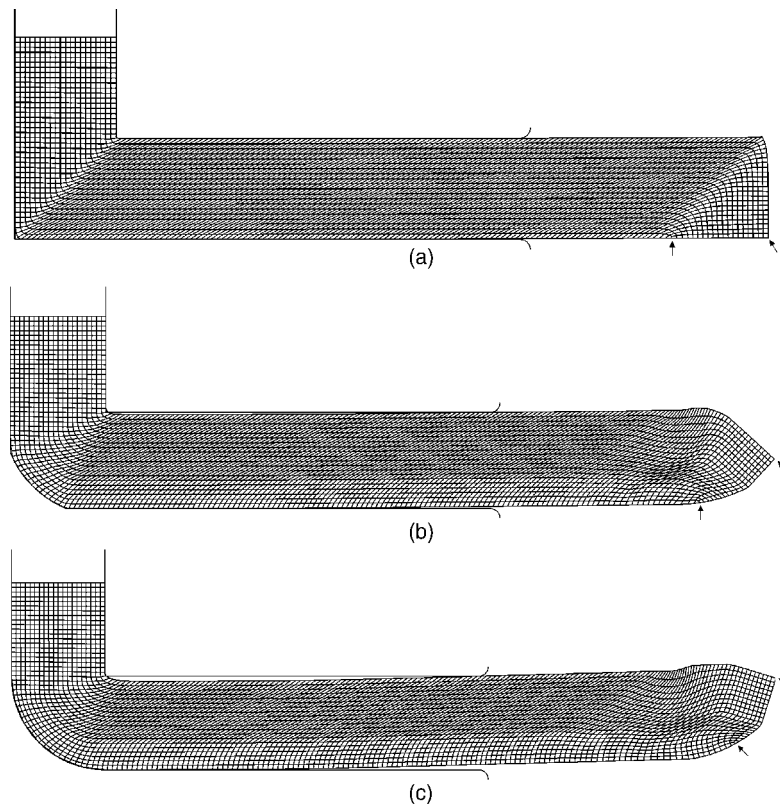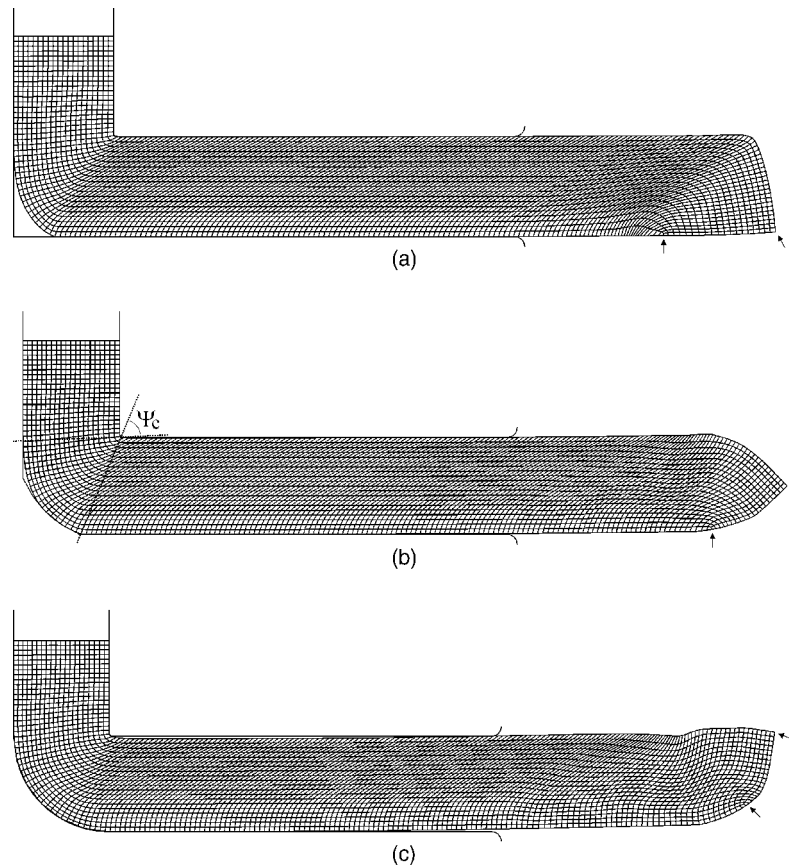

Fig. 5. Influence of outer corner angle Ψ on the deformed meshes of the billets and material fill status for (a) case 1, $\Psi = 0°$; (b) case 2, $\Psi = 45°$; (c) case 3, $\Psi = 90°$. The front surface of the billet is indicated as the area between the two arrows in each case.

Fig. 6. Influence of outer corner angle Ψ on the deformed meshes of the billets and material fill status for (a) case 4, $\Psi = 0°$; (b) case 5, $\Psi = 45°$; (c) case 6, $\Psi = 90°$. The front surface of the billet is indicated as the area between the two arrows in each case.

Kim et al. [12] for AA1100 and AA6061 alloys and Moon et al. [14] in peak- and under-aged 6061 Al alloys. Also in agreement, they observed that in the same ECAE condition, the corner gap was less pronounced in materials with less work hardening.

3.1.2. Strain inhomogeneity

Figs. 7 and 8 show the distributions of the equivalent plastic strain, $\bar{\varepsilon}^p$, in the billets simulated with the different Ψ, respectively, for the two materials. In all cases, the deformation varies both along the billet axis and along the transverse direction from top to bottom.

Along the billet axis from left to right, there are three distinct deformation regions: tail, steady state, and head. The length of the non-uniformly deformed tail part is similar for the different cases. The length of the head region scaling with billet w, however, varies with the material and Ψ. For the PP material, it increases with Ψ equaling $\sim$1.3w in the case of $\Psi = 0°$ (Fig. 7a), $\sim$1.8w for $\Psi = 45°$ (Fig. 7b), and $\sim$2.1w for $\Psi = 90°$ (Fig. 7c). In the SH material (Fig. 8), the lengths of the head region are similar for the different Ψ, being $\sim$2.8w, much greater than those seen in the PP material.

Between the inevitable non-uniformly deformed head and tail regions, there is clearly a steady-state region where the strain is uniform along the axis. Within this steady-state re-

gion, however, deformation inhomogeneity still exists along the transverse direction (e.g. bottom to top along the width) to a degree that varies with material and Ψ. Table 2 shows the change in the strain $\bar{\varepsilon}^p_{ave}$, averaged across the billet from top to bottom. Due to the formation of regions of little to no intense shearing as the outer corner becomes rounded, $\bar{\varepsilon}^p_{ave}$ decreases with Ψ. For $\Psi = 0°$, $\bar{\varepsilon}^p_{ave}$ is higher for case 1 (and 7) and decreases with strain hardening as a corner gap forms, but for $\Psi > 0°$ it increases with strain hardening.

For better recognition of strain inhomogeneity than analyzing averages, Fig. 9 shows the distributions of $\bar{\varepsilon}^p$, plotted

Table 2
Average equivalent plastic strain across the billet width $\bar{\varepsilon}^p_{ave}$, deformation inhomogeneity index C_i (Eq. (5)) and effective outer corner angle Ψ_e (see Figs. 1b and 6b) of the billets simulated without and with friction

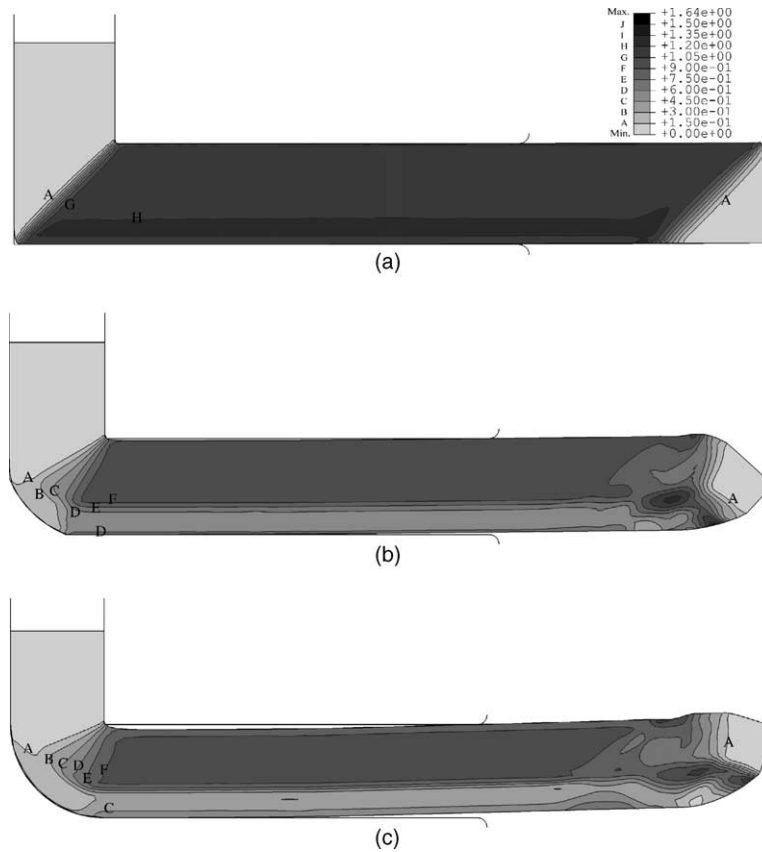| Material	Ψ (°)	$\mu = 0$			$\mu = \mu_m$		
		$\bar{\varepsilon}^p_{ave}$	C_i	Ψ_e (°)	$\bar{\varepsilon}^p_{ave}$	C_i	Ψ_e (°)
Perfectly plastic	0	1.157	0.18	0	1.171	0.23	0
	45	0.854	0.54	45	0.869	0.56	45
	90	0.757	0.85	90	0.763	0.88	90
Strain hardening	0	0.945	0.70	54	1.032	0.71	33
	45	0.869	0.80	65	0.902	0.69	60
	90	0.801	0.87	90	0.836	0.90	90

Fig. 7. Influence of outer corner angle Ψ on the distribution of equivalent plastic strains in the billets for (a) case 1, $\Psi = 0°$; (b) case 2, $\Psi = 45°$; (c) case 3, $\Psi = 90°$.

as a function of the relative distance to the top surface of the billet d/w, where d is the distance to the top surface and w (=10 mm) is the initial width of the billet. The von Mises equivalent plastic strains calculated according to Eqs. (1) and (2) are also shown in this figure for comparison. For the PP material (Fig. 9a), the strain distribution along the billet width is nearly uniform for $\Psi = 0°$, but notably non-uniform for $\Psi = 45°$ and $90°$. For $\Psi = 45°$ or $90°$, however, the distribution of $\bar{\varepsilon}^p$ is uniform in the upper region from the top surface ($d = 0$) to the vicinity of $d/w = \sim 2/3$. From there on to the bottom surface of the billet, $\bar{\varepsilon}^p$ first decreases significantly with d/w, reaching a minimum at $d/w = \sim 0.9$ for $\Psi = 45°$ and at $d/w = \sim 0.8$ for $\Psi = 90°$, and then increases again until $d/w = 1$. The $\bar{\varepsilon}^p$ values in this lower region ($d/w = \sim 2/3$ to 1) are much smaller than those in the more uniformly deformed upper region ($d/w = 0$ to $\sim 2/3$). Also the deviation in plastic strain in the lower part and the uniformly deformed upper region is greater in the case of $\Psi = 90°$ than that for $\Psi = 45°$, though the size of the lower portion is the same.

In the SH material (Fig. 9b), the magnitude of $\bar{\varepsilon}^p$ decreases with Ψ, but the strain profiles across the billet for different Ψ are similar. Apart from the local variations at the die-billet interfaces, there is no section of uniform $\bar{\varepsilon}^p$, as it essentially decreases from the top to the bottom of the

billets unlike in the PP case. Particularly for $\Psi = 0°$, $\bar{\varepsilon}^p$ in the central region is substantially reduced due to the formation of a corner gap. Also the effect of Ψ on the strain distribution is significant over a larger region of the material, approximately from $d/w = \sim 0.6$ to 1, where the minimum $\bar{\varepsilon}^p$ is located, for all values of Ψ.

For case 1 only, the theoretical value calculated from Eq. (1) matches the average level of the FE predicted $\bar{\varepsilon}^p$ well. For all remaining cases, it does not. For $\Psi > 0°$, Eq. (2) underestimates the strain levels in the uniformly deformed upper regions, and overestimates it in the lower regions.

To quantify the degree of deformation inhomogeneity along w, a deformation inhomogeneity index C_i, defined by

$$C_i = \left(\frac{\bar{\varepsilon}^p_{\max} - \bar{\varepsilon}^p_{\min}}{\bar{\varepsilon}^p_{\text{ave}}} \right) \tag{5}$$

where $\bar{\varepsilon}^p_{\max}$, $\bar{\varepsilon}^p_{\min}$, and $\bar{\varepsilon}^p_{\text{ave}}$ denotes, respectively, the maximum, minimum, and average of the equivalent plastic strains along the billet width, was calculated for each case and is shown in Table 2. In summary, if no corner gap forms, strain inhomogeneity along w increases with Ψ and with the hardening rate (SH versus PP).
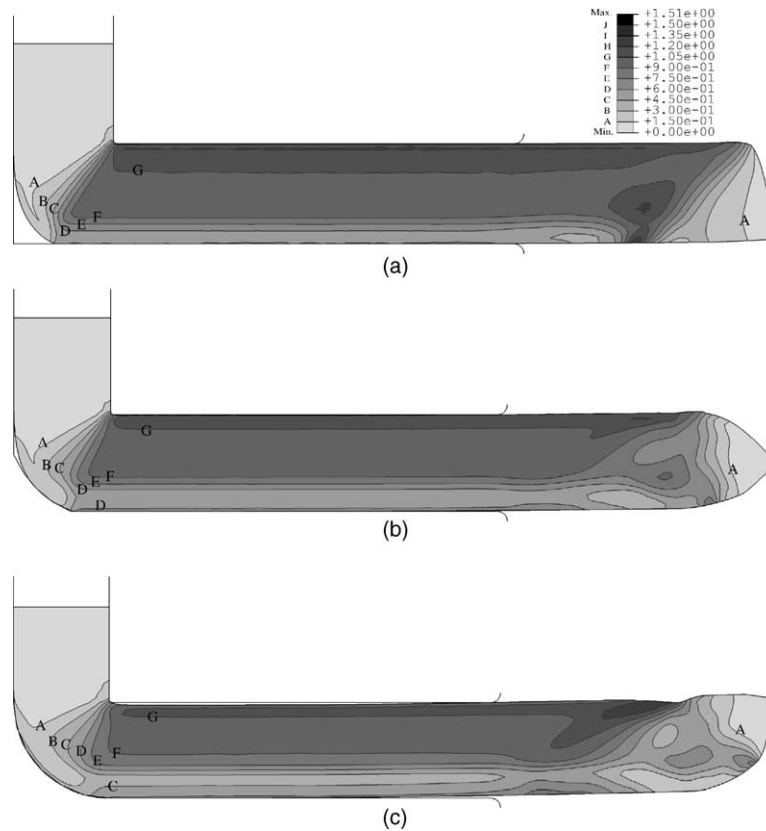
Fig. 8. Influence of outer corner angle Ψ on the distribution of equivalent plastic strains in the billets for (a) case 4, $\Psi = 0°$; (b) case 5, $\Psi = 45°$; (c) case 6, $\Psi = 90°$.

3.1.3. Plastic deformation zone (PDZ)

Trends in the degree of inhomogeneity originate in PDZ development. For these reasons, the morphology and strain-rate distribution within the PDZ, two chief characteristics of the PDZ, are addressed here. The PDZ generated in steady state is assessed in two ways using a yield indicator and plastic strain-rate.

The yield indicator provides information on the shape of the PDZ and equals 1 if plastic deformation takes place or 0 if not. It is recorded at each integration point for each time (or strain) increment. An effective yield indicator for an element i, say Y_i, is then calculated as the average of the individual values at its associated integration points. The elements used in these simulations have four integration points. Therefore, Y_i equals 0.25, 0.5, 0.75, or 1 if plastic deformation occurs at one, two, three, or all integration points, respectively. Under frictionless conditions, Fig. 10 shows the field of effective yield indicator values obtained at the last strain increment. In this figure, the elements that are fully plastically deformed (i.e. $Y_i = 1$) are plotted in grey, whereas those only partially plastically deformed (i.e. $0 < Y_i < 1$) are plotted in black (around the corresponding integration points) and those elastically or not deformed ($Y_i = 0$) are white. In this way, the grey and black areas together define the shape of the PDZ.

Fig. 10 compares the effects of Ψ and material response on the shape of the PDZ. For a given material, as Ψ increases from $0°$ to $90°$, the PDZ becomes broader and splits into two parts near the two ends of the arc at the outer die corner (points A and B in Fig. 1a). In the center of the outer corner (O' in Fig. 1a), there is no plastic deformation, indicating rigid body rotation.

For $\Psi = 0°$, we observe the greatest influence of material response due to the formation of the outer corner gap. For the PP material and $\Psi = 0°$ (Fig. 10a), the PDZ is a narrow banded region around the intersection plane (line OO' in Fig. 1a) of the two channels. In the SH material, however, the central PDZ (i.e. PDZ in the intersectional area) is much broader, nearly as broad as the case of $\Psi = 45°$. In contrast for $\Psi = 45°$ and $90°$ (Fig. 10b and c versus Fig. 10e and f), the material nearly or completely fills the die and hence the shape of the PDZs are very similar between the two materials for the same Ψ.

Plastic deformation in the inlet and outlet channels appears to be more extensive in the SH case than the PP case. In the former, plastic deformation encompasses large areas of the inlet channel and of the entry of the outlet channel close to the bottom die wall (Fig. 10d–f). In the PP case, the PDZ does expand a little to the right of the inner die corner and plastic deformation also occurs in the inner side of the
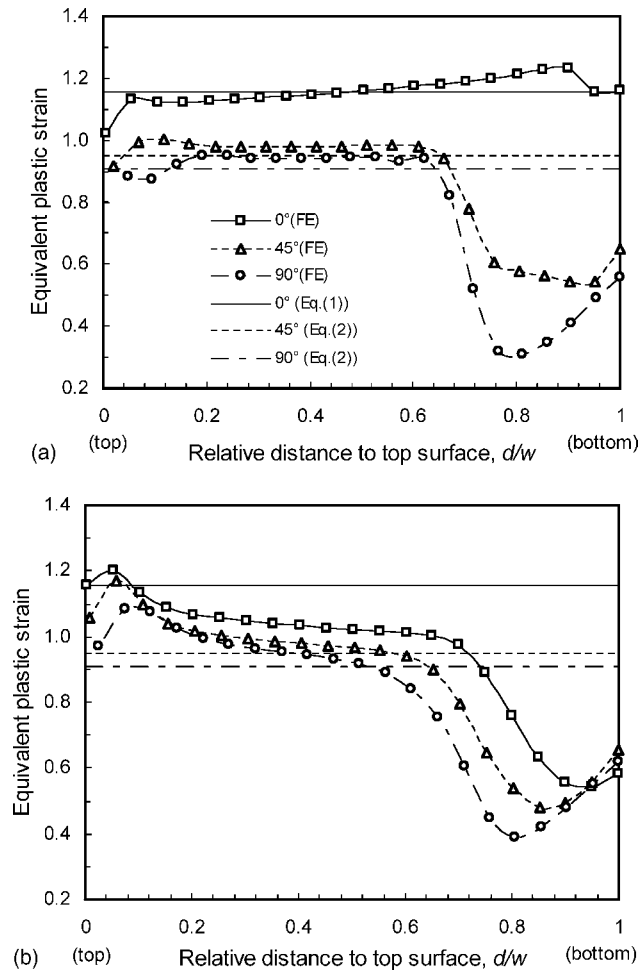
Fig. 9. Influence of Ψ on the variation of equivalent plastic strain along the billet width in the steady-state region of the billets (a) PP cases 1–3 and (b) SH cases 4–6. The theoretical values calculated using Eqs. (1) and (2) are shown for comparison.

inlet channel, but overall, inlet and outlet channel deformation is less extensive.

Recall that the distribution of the yield indicator indicates only where plastic deformation has taken place during the strain increment and does not provide any quantitative information about the magnitude of plastic deformation. In other words, it shows the shape of the PDZ, but does not reveal the spatial variation of plastic deformation within it. To show the latter, we also report the plastic strain-rate field.

Fig. 11 shows the distribution of the equivalent plastic strain-rate $\dot{\varepsilon}^p$ for the two materials ECAE'ed with different Ψ. Note that a minimum level of $\dot{\varepsilon}^p$ (non-zero) had to be chosen in plotting these results, i.e. 0.05 in Fig. 11. As a result, (1) the PDZ represented by the $\dot{\varepsilon}^p$ in this figure appears smaller than that identified by yield indicators in Fig. 10, yet still has a similar shape, (2) plastic deformation in the inlet channel is removed from the PP material but not the SH material, and (3) relative magnitudes of $\dot{\varepsilon}^p$ can be studied to reveal the symmetry of the PDZ.

For case 1 [PP, $\Psi = 0°$, $\mu = 0$] (Fig. 11a), the highest $\dot{\varepsilon}^p$ is located along the intersection plane of the channels, which indicates that most of the plastic deformation takes place in this region. $\dot{\varepsilon}^p$ in this region is higher at the outer and inner corners than in the central area; the central area is broader and consequently the total plastic strain remains almost uniform along the billet width (see Fig. 9a). For cases 2–6 (Fig. 11b–f), the PDZ consists of three regions: one is the central fan emanating from the inner die corner, and the other two are located in the bottom portion bounding the zone of rigidly rotating material. When corner gaps form, they are located where the material separates from the die, whereas when the material fills the die, they are located approximately where the channels mate with the rounded corner.

Comparison of the PDZ between the two materials indicates that the difference is most significant for the case of $\Psi = 0°$ (Fig. 11a and d), and becomes negligible for $\Psi = 90°$ (Fig. 11c and f). For $\Psi = 0°$, a large corner gap is formed in the SH case. This free surface splits the PDZ into three regions as if $\Psi > 0°$, that is, a fan-like upper region and a lower region whose local maxima in $\dot{\varepsilon}^p$ occur at the two ends of the corner gap rather than the ends of the rounded corner. Another difference is that the SH material shows noticeable plastic deformation in the inlet channel.

In Fig. 11, the local maxima of $\dot{\varepsilon}^p$, at the upper region (central fan) and lower region, are indicated in the figure for the convenience of inspecting the variation of strain-rate with Ψ and material. The local maxima in the upper region are located at the inner corner and in the lower region, at the outer surface. For a given material, these maxima decrease with Ψ. In cases where a corner gap forms, cases 4 and 5, the PDZ is asymmetric. In these cases, the local maximum of $\dot{\varepsilon}^p$ is noticeably higher at the finishing end of the outer corner arc than at the starting end. In other cases where a corner gap does not form, e.g. $\Psi = 90°$ (Fig. 11c), the distributions of $\dot{\varepsilon}^p$ become very symmetrical with respect to the intersect plane, regardless of material behavior. For $\Psi = 0°$ (Fig. 11a), the single local maximum $\dot{\varepsilon}^p$ at the sharp outer corner might be considered as a result of degeneration of the arc (AB in Fig. 1a) to a single point (O' in Fig. 1a) at the outer corner when Ψ decreases to 0°. Thus, in case 1, the central PDZ appears as one region, instead of three regions, as in the cases of $\Psi = 45°$ or 90°.

3.1.4. Comparison with similar FE studies

There are a few other FE studies that consider PDZ development for a subset of the simulations performed here though they are not exact replications. In [13], the effects of strain hardening and strain-rate sensitivity on the PDZ were assessed by considering model materials with stress–strain relationship of $\sigma = \varepsilon^n \dot{\varepsilon}^m$ and varying the strain hardening exponent n and the strain-rate sensitivity m, for frictionless tooling with $\Phi = 90°$ and $\Psi = 0°$. The characteristics of the PDZ for their rigid PP material ($n = 0$, $m = 0$) [13] are very similar to our results for $\Psi = 0°$ (Fig. 11a). However for the
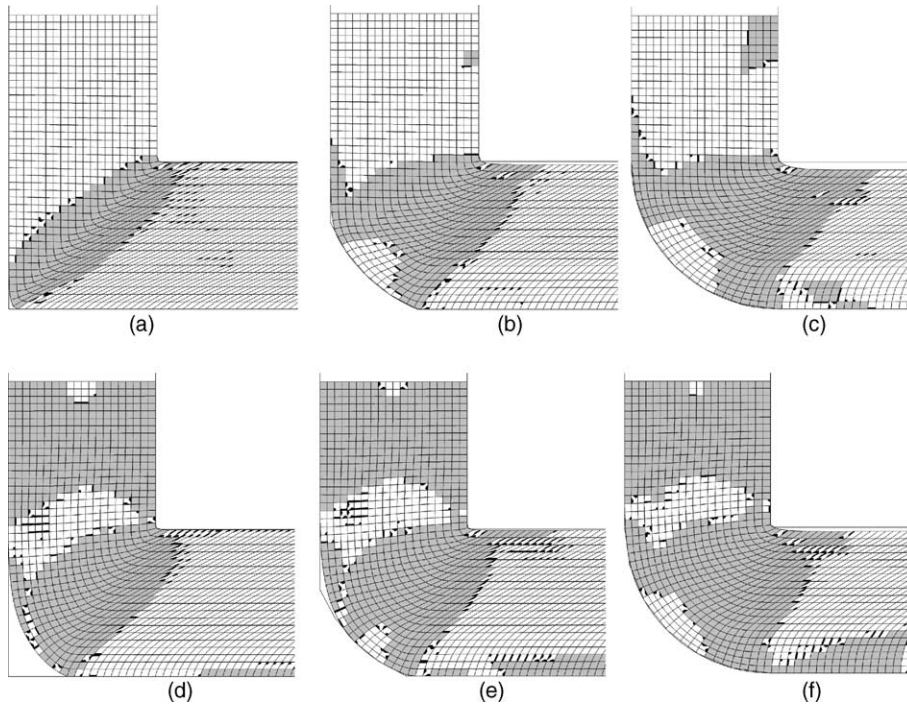
Fig. 10. Comparison of the shape of the PDZ as revealed by yield indicators (Y_i) simulated for (a–c) cases 1–3, respectively, and (d–f) cases 4–6, respectively. The elements in grey and black are fully ($Y_i = 1$) and partially ($0 < Y_i < 1$) plastically deformed.
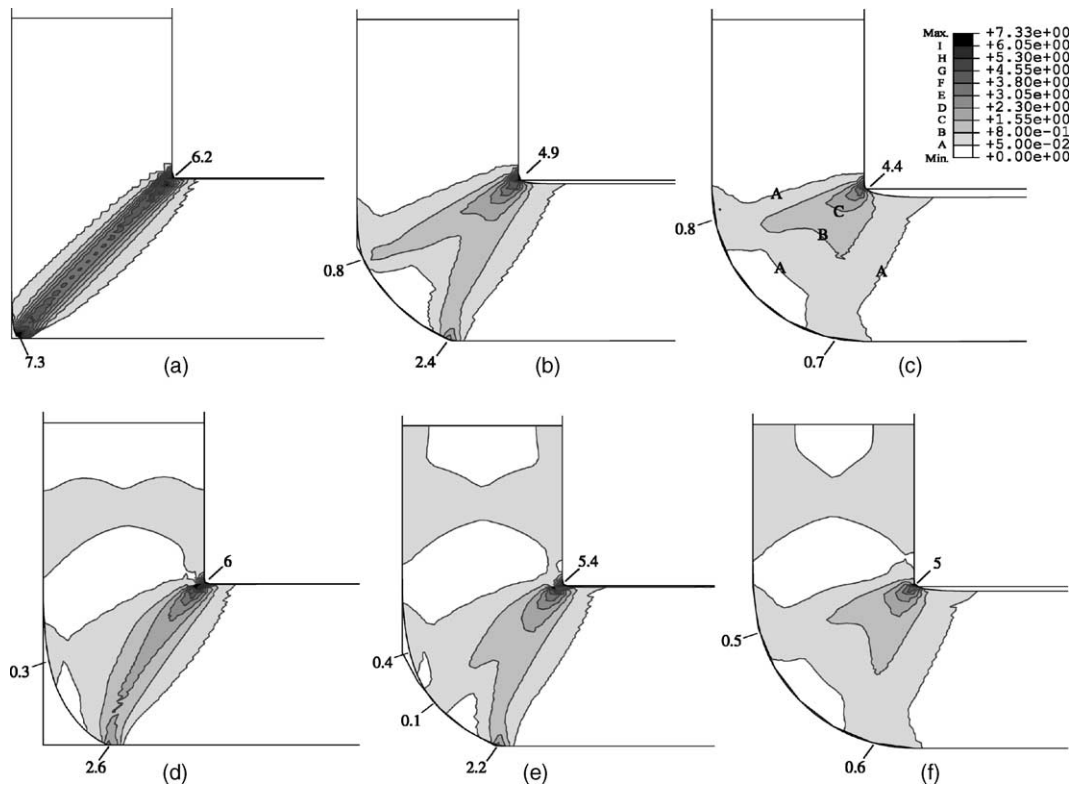

Fig. 11. Comparison of the distribution of equivalent plastic strain-rate (s^{-1}) within the PDZs for (a–c) cases 1–3, respectively, and (d–f) cases 4–6, respectively.
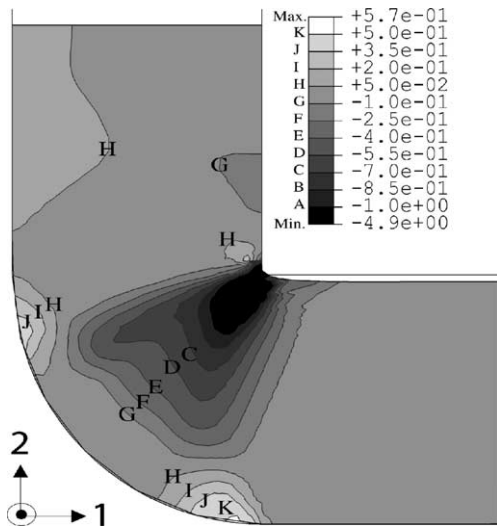
Fig. 12. Spatial variation in the plastic strain-rate component $\dot{\varepsilon}_{22}$ (s^{-1}) within the PDZ to reveal the sign reversal between the upper fan-like region and the lower region for case 6 [SH, $\Psi = 90°$, $\mu = 0$]. Table 3 shows an estimate of $\beta = {\sim}49°$ for the central fan in the upper region.

strain hardening material ($n = 0.5$, $m = 0$), their results [13] do not show the splitting of the deformation zone at the outer corner and the extension of the deformation zone in the inlet channel as observed in our results (see Fig. 11d). This might be due to the selection of a relatively high minimum level of strain-rate used in their plot. The yield indicator results presented here confirm that the PDZ splits into two regions separated by a zone with no plastic deformation around the center of the arc (see Fig. 10c). Kim [19] also investigated the effect of Ψ on the PDZ in a rigid PP material using dies with $\Phi = 90°$ and $\Psi = 0°$, $45°$ or $90°$, respectively. Except for the case of $\Psi = 45°$,[2] his results are comparable to ours.

Previous discussions of deformation in the outer corner region (e.g. [18,26]) were mostly based on the element distortions or stress distributions. In fact, the deformation type can be more easily (and also more reliably) recognized and quantitatively assessed by examination of the distribution of individual components of the plastic strain-rate. Fig. 12 shows, for example, the distribution of the plastic strain-rate component in the vertical direction $\dot{\varepsilon}_{22}$ in the billet for the SH material and $\Psi = 90°$ in fixed global coordinates. Evidently, $\dot{\varepsilon}_{22}$ is positive around the starting and finishing ends of the arc at the outer curvature of the billet. Equivalently along a flow line, the billet experiences tensile deformation around the starting point A in Fig. 1a when it enters the outer corner region and then compression deformation around point B when it exits the outer corner region. The tensile and compression deformations can be attributed to changes in flow direction from a positive curvature (convex) to negative curvature (concave) when the material flows along the rounded

corner. In agreement, Bowen et al. [15] detected tensile and then compressive deformation near the outer surface of the billet based on measurements of experimental grid distortions on an Al sample ECAE'ed under low friction conditions, although it was for a $\Phi = 120°$ die. It can also be seen from Fig. 12 that in the inlet channel, the left and right sides of the billet undergo, respectively, tensile and compressive deformation along the channel axis direction. Similar characteristics of plastic strain-rate distributions and deformation types in the outer corner and inlet channel regions also exist for the other cases, except for case 1.

3.2. Effect of friction

FE simulations thus far were frictionless. To study the additional effects of friction, the maximum "applicable" friction coefficient μ_{m} had to be determined for each case in cases 7–12. μ_{m} is defined as the maximum value of μ such that (i) the FE simulation can be completed and (ii) steady state is achieved and the central portion of the billet is uniformly deformed. μ_{m} depends on the length of the exit channel L_{e} and the length of the billet L_{b}, increasing if either (or both) of these lengths is decreased and leads to a reduction in the contact surface between the billet and the channel. For instance, if FE simulations are carried out with $\mu = \mu_{\mathrm{m}} + 0.025$, then localized deformation would develop at the surface of the billet, resulting in either a completed simulation but without a steady-state uniform region or a prematurely failed simulation. By reducing L_{b} or L_{e} for the same μ, the area over which friction acts and hence the total accumulated friction force are reduced, potentially leading to a completed simulation with steady state. As an example, Fig. 13 shows the distribution of $\bar{\varepsilon}^{\mathrm{p}}$ in the billets for three simulations performed for the case of a SH material and $\Psi = 0°$, using different L_{b} and L_{e}. Fig. 13a shows that with $\mu = 0.1$, the simulation with current die geometry (with $L_{\mathrm{b}} = 8.3w$ and $L_{\mathrm{e}} = 4.0w$), was completed without a steady-state region in the billet. Highly localized plastic deformation forms in the bottom region of the billet close to the outer corner of the die. However, the simulation with the same μ clearly reaches steady state when either L_{e} was reduced to w (Fig. 13b) or L_{b} was reduced to $5.8w$ (Fig. 13c).

In the following, the results obtained from the FE simulations using the associated μ_{m} for each case for $L_{\mathrm{b}} = 8.3w$ and $L_{\mathrm{e}} = 4w$ are compared with those for the frictionless cases. The effect of μ on the loading force is discussed in Section 3.3.

3.2.1. Effect of friction on overall deformation behavior and strain inhomogeneity

Figs. 14 and 15 show the distribution of $\bar{\varepsilon}^{\mathrm{p}}$ in the deformed billets associated with cases 7–12. Generally, the μ_{m} coefficients are different for each case. μ_{m} tends to increase with Ψ, which is reasonable because the rounded corner eases pressing, allowing for higher allowable friction conditions. Still these allowable friction coefficients are much lower

---

[2] The outer corner of the die in Figs. 3c or 4c in [19] suggests that the outer corner angle $45°$ may be defined differently from our die, as there are no outer surface discontinuities in [19].
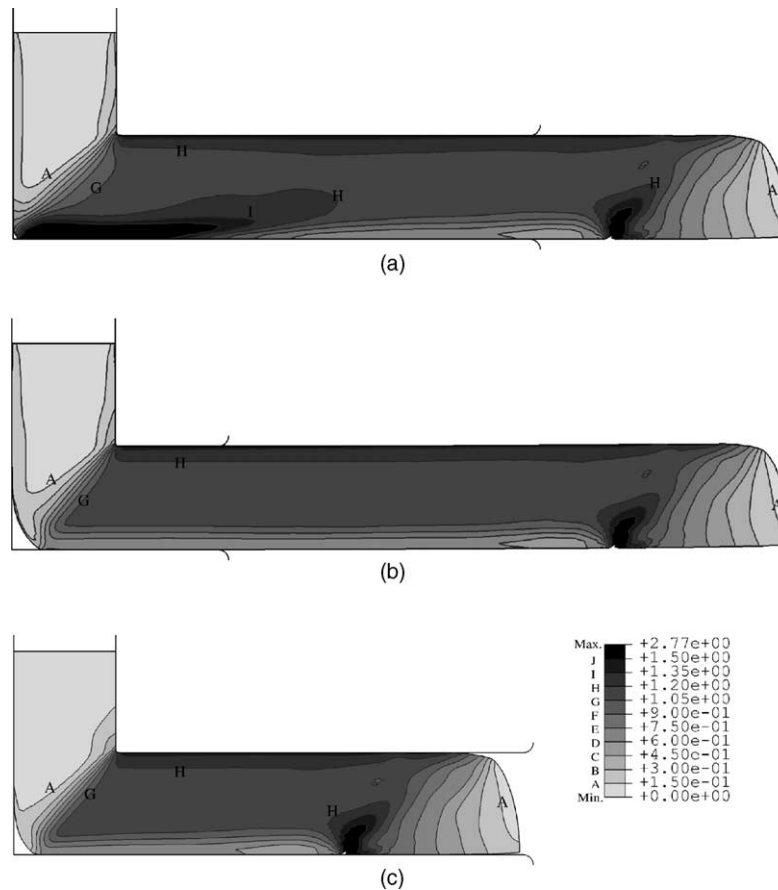
Fig. 13. The effect of billet length (L_b) and exit channel length (L_e) on the ability of the simulation to achieve a steady-state distribution of equivalent plastic strains for an example case with friction [SH, $\Psi = 0°$, $\mu = 0.1$]. As shown no steady state for (a) $L_b = 8.3w$, $L_e = 4w$, but steady state for (b) $L_b = 8.3w$, $L_e = w$ and (c) $L_b = 5.8w$, $L_e = 4w$.

than those that can be tolerated in other forming processes such as rolling and deep drawing, suggesting that better lubrication conditions need to be maintained in ECAE.

By comparing Figs. 14 and 15 to those for the frictionless conditions (Figs. 7 and 8) the influence of friction on the deformation is apparent. First, friction reduces the corner gap size, which can be attributed to the increased constraint force at the billet surface. Based on the Ψ_e provided in Table 2 for $\mu = \mu_m$, this effect is only relevant in SH materials for $\Psi = 0°$ and $45°$. For $\Psi = 90°$, no distinguishable gaps can be seen for cases 3, 6, 9, and 12. Secondly, friction reduces the upward bending of the billet and results in smaller gaps in the outlet channel. This can be seen for $\Psi = 45°$ (Figs. 7b and 14b) and $90°$ (Figs. 7c and 14c) in the PP material and for $\Psi = 90°$ (Figs. 8c and 15c) in the SH material.

Thirdly, plastic deformation increases locally when friction exists. Fig. 16 compares the distribution of $\bar{\varepsilon}^p$ versus d/w in the steady-state region for the billets simulated with and without friction. When no corner gap forms, friction changes $\bar{\varepsilon}^p$ only locally in the top and bottom surface regions and not the central region, regardless of Ψ and material response. For instance, for $\Psi = 0°$ (Fig. 16a), only $\bar{\varepsilon}^p$ in the bottom region of the billet increases when μ increases

from 0 to 0.025, whereas for $\Psi = 45°$ (Fig. 16b) and $90°$ (Fig. 16c) $\bar{\varepsilon}^p$ in both the top and bottom regions increases with μ. In contrast, when a corner gap forms, as for cases 4 and 5 (Fig. 16d and e), friction leads to higher $\bar{\varepsilon}^p$ not only in the surface regions but also in the middle region (along the width) of the billets.

Lastly, in most cases, inhomogeneity in strain increases with friction. As shown in Table 2, the deformation inhomogeneity index C_i appears to increase with μ in all cases, except case 11. The decrease of C_i with friction in this case can be attributed to the more significant increase in $\bar{\varepsilon}^p_{min}$ than in $\bar{\varepsilon}^p_{max}$ (Fig. 16e). These results suggest that the thought of reducing strain inhomogeneity across the billet width by increasing the friction between the billet and the die wall (e.g. [18]) seems to be inapplicable in most cases.

3.2.2. Effect of friction on the PDZ

Fig. 17 shows the distribution of the equivalent plastic strain-rate $\dot{\varepsilon}^p$ in the billets simulated with $\mu = \mu_m$ (cases 7–12) using the same scales as in Fig. 11. Comparing Fig. 17 to Fig. 11 reveals that friction does not significantly affect the shape, when the material fills the die corner (i.e. cases 1–3, 5–9, 11, and 12), but does affect the strain-rate distribution in
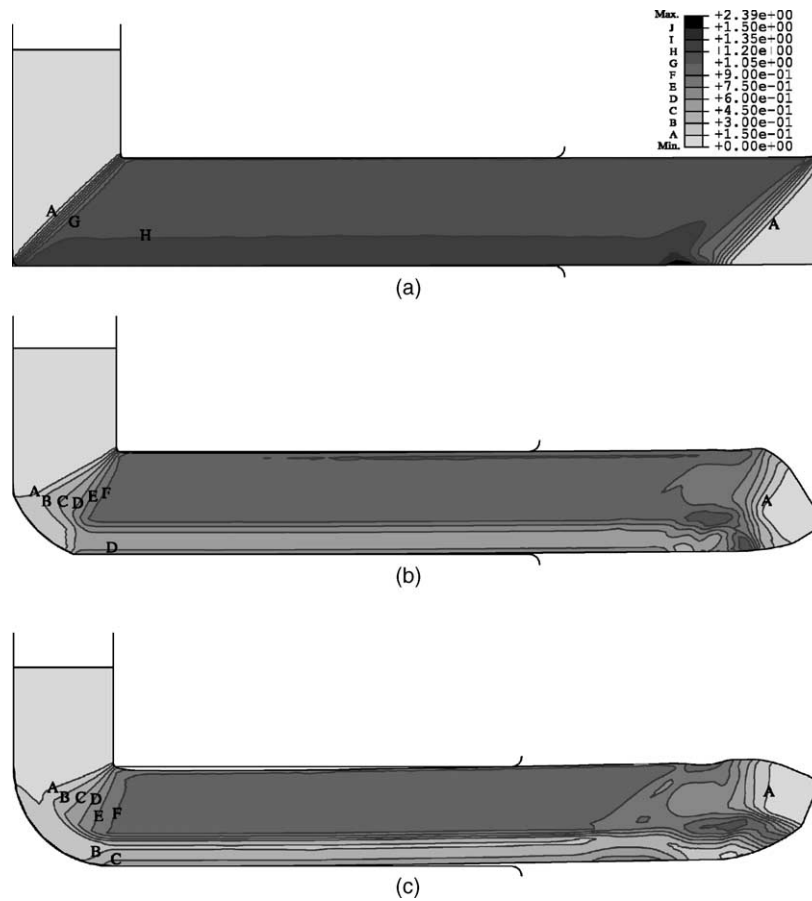
Fig. 14. Combined influence of Ψ and μ on the distribution of equivalent plastic strains for cases 7–9 (a–c), respectively.

the PDZ. This friction effect can be seen from the variation of the local maxima in $\dot{\varepsilon}^p$ at the inner and the outer corner regions. In all the cases, the maximum $\dot{\varepsilon}^p$ at the inner corner increases with the friction, most significantly in case 10. On the other hand, variation of the local maximum $\dot{\varepsilon}^p$ in the outer corner region with friction appears to be sensitive to Ψ and material behavior. For $\Psi = 0°$, friction leads to increases in the maximum of $\dot{\varepsilon}^p$ at the outer corner in the case of the PP material (compare Figs. 11a and 17a) and near the finishing end of the arc at the outer curvature in the SH material (Fig. 11d versus Fig. 17d). For $\Psi = 45°$, the distribution of strain-rate in the PDZ becomes more symmetric and less dependent on material response as friction helps to reduce the corner gap in the SH case. For the case of $\Psi = 90°$, the material easily fills the die with and without friction and hence there is no significant change of $\dot{\varepsilon}^p$ at the outer corner region in both materials (Fig. 11c versus Fig. 17c; Fig. 11f versus Fig. 17f).

The effect of friction on the plastic strain-rates as stated above translates directly with its effect on the accumulated plastic strains. For example, the friction-induced higher equivalent plastic strains in the bottom of the billet in the case of PP material with $\Psi = 0°$ (Fig. 16a) can be attributed to the higher plastic strain-rate when the material passes the outer corner (Fig. 17a).

3.2.3. Characterizing the PDZ

Understanding ECAE deformation can be directly linked to an understanding of PDZ development, which, in turn, depends on several factors, including die geometry. Eq. (1) by [2] and Eq. (2) by [6] predict the effective strain based on the die geometry, whereas Eq. (3) by [9] predicts it based on a central fan PDZ. Eq. (1) works well in the case of $\Psi = 0°$ and as expected when the material is PP, as demonstrated in Fig. 9. In all other cases, Eq. (2) underestimates the strain in the uniformly deformed upper region.

Better predictions of strain can be estimated when the shape of the PDZ is considered. As demonstrated in [5,9], simple shear on an intersection plane, Eq. (1) and a central fan PDZ, see Fig. 1b and Eq. (3), provide uniform deformation. Consequently in order for a die with nonzero Ψ or with a free surface corner gap to result in inhomogeneous deformation, the associated PDZ can neither be simple shearing nor entirely fan-like. Thus, for $\Psi > 0°$, a fan PDZ would best represent only the upper portion of the PDZ. To show this, the effective plastic strains in Fig. 16 in the upper region are matched with Eq. (3) to determine an "effective β", displayed in Table 3. As shown, the effective angle β increases with Ψ, and generally Ψ and β are not equal. Table 3 also suggests that the PDZ broadens with corner gap formation: β is nonzero for SH cases 4 and 10, in which a sizable corner
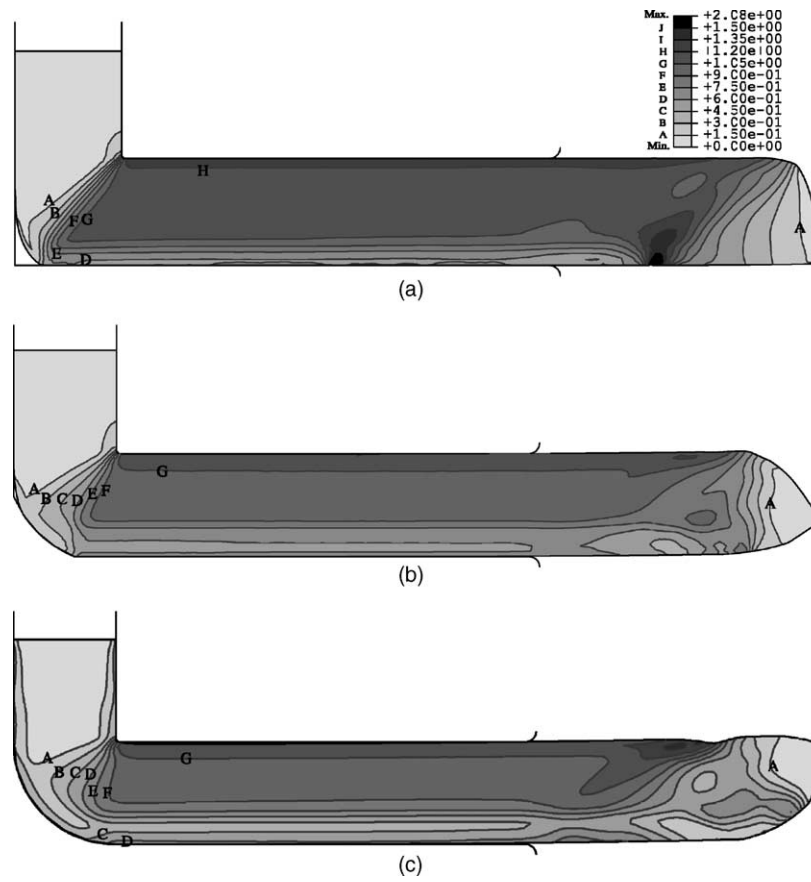
Fig. 15. Combined influence of Ψ and μ on the distribution of equivalent plastic strains for cases 10–12 (a–c), respectively.

gap formed, but zero for the corresponding PP cases 1 and 7, in which little to no corner gap formed. Otherwise, in the remaining cases, when the material mostly fills the die, β is larger for the PP material than SH material. In addition, for the PP cases, 1–3 and 7–9, friction seems to have no influence on β, whereas for a SH material, friction decreases β.

3.3. Load–displacement curves

Figs. 18 and 19 show the simulated load–displacement curves for the SH ($\mu = 0.075$) and PP material ($\mu = 0.025$), respectively, for different Ψ in each figure. According to analyses by Segal [4] and Lee [8], the pressing pressure P in ECAE of an ideal PP material under frictionless conditions

can be calculated by

$$P = 2k \cot \left(\frac{\Phi}{2} \right) \tag{6}$$

where k is the shear yield stress of the material. Accordingly, the load F can be calculated as

$$F = P \times A \tag{7}$$

where A is the cross-sectional area of the billet. As shown in Fig. 19a, this solution indeed only applies to case 1. In all other cases studied here, the force is not constant with displacement. Material response and friction tend to control the magnitude of the force, which increased with μ and material flow stress, whereas Ψ controlled the characteristics of its evolution with ram displacement.

Curves for $\Psi = 0°$ evolve differently than those for $\Psi = 45°$ or $90°$, which are quite similar. Therefore in the following, trends of working load development in the different stages only for $\Psi = 0°$ and $90°$ (indicated on Fig. 18a) are explained in association with the deformed configurations in Figs. 20 and 21 at the transition points between the stages.

For the case of $\Psi = 0°$, four stages can be distinguished (Fig. 18a). In Stage I, the load increases rapidly with the displacement reaching a maximum. This stage begins when the head of the billet first touches the bottom wall of the die

Table 3
Effective value of β for a fan-like PDZ estimated from fitting Eq. (3) with the effective strains in the upper region in Fig. 16

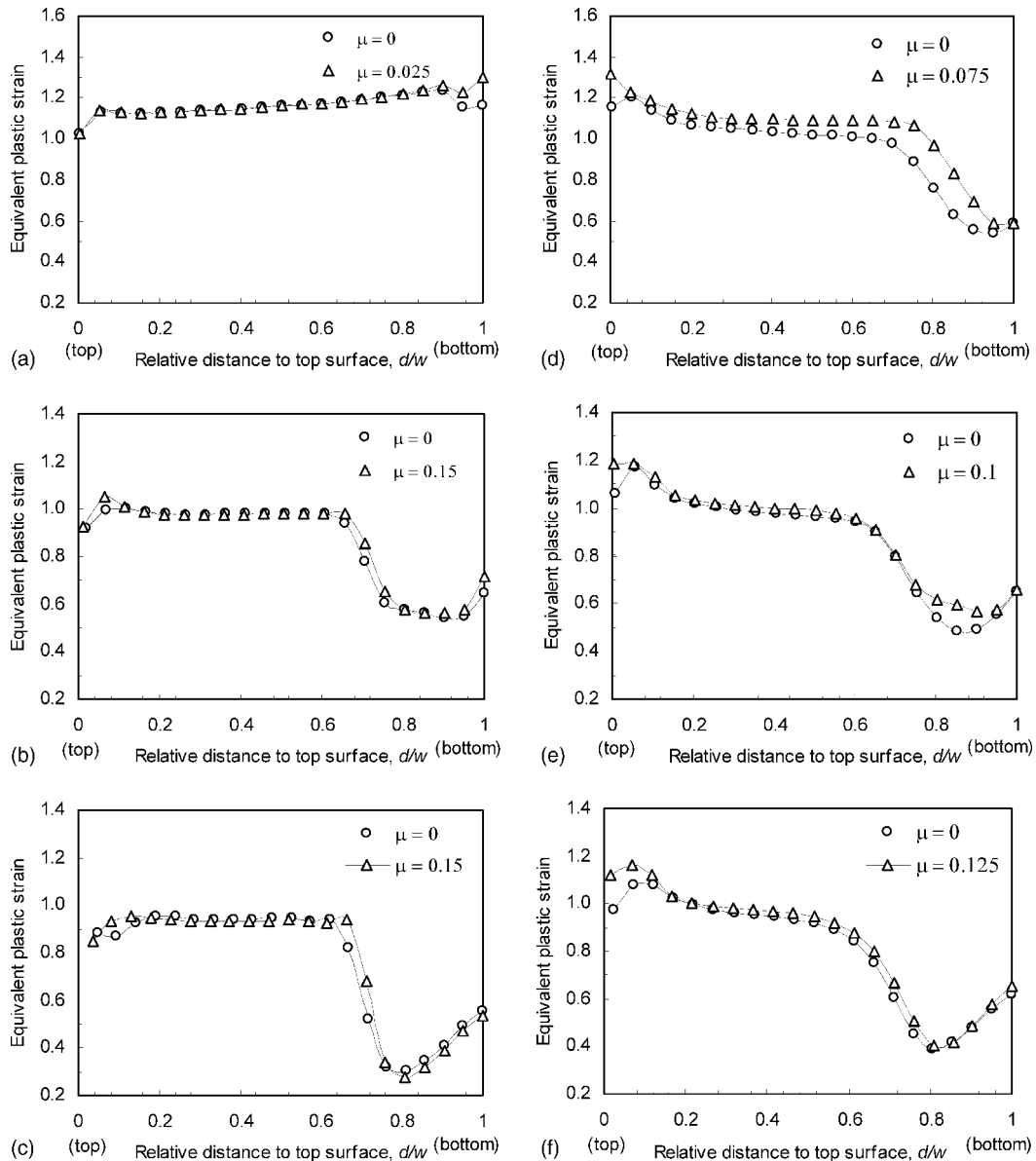| Material	Ψ (°)	$\mu = 0$ (°)	$\mu = \mu_m$ (°)
Perfectly plastic	0	0	0
	45	46	46
	90	49	49
Strain hardening	0	34	22
	45	42	39
	90	49	45

Fig. 16. Influence of friction coefficient μ on the equivalent plastic strain distributions along the billet width in the steady-state region for (a) cases 1 and 7, (b) cases 2 and 8, (c) cases 3 and 9, (d) cases 4 and 10, (e) cases 5 and 11, and (f) cases 6 and 12.

and involves its severe deformation as it bends around the die corner (Fig. 20a). In Stage II, the load decreases from the maximum to a local minimum, followed by a small increase in Stage III. During these transient stages, the non-uniform region at the head end is developing (Fig. 20b). In Stage IV the load remains almost constant with displacement until the end of the ECAE pass. Fig. 20c shows the transition from Stage III to Stage IV is the moment when the non-uniformly deformed billet head completely moves out of the deformation zone. Comparing Fig. 20c with Fig. 8a shows that the beginning of Stage IV is also the moment the process enters into steady state.

For $\Psi = 45°$ and $90°$, five stages can be distinguished (Fig. 18a) instead of four. In Stage I, the load increases

rapidly with the ram displacement. This stage starts from the moment the front surface of the billet starts to contact the curved die wall at the outer corner and ends when the billet head bends over the rounded corner (Fig. 21a). Stage II is featured by a small increase of the load, and the end of this stage is when the upper surface of the billet begins to touch the upper wall of the outlet channel (Fig. 21b). The slow increase of load in this stage might be explained by the lack of constraint on the billet head. Stage III is the period from the moment the billet head touches the upper wall of the outlet channel (Fig. 21b) to the moment that sufficient contact is established between the upper surface of the billet head and the upper wall of the outlet channel (Fig. 21c). The rapid increase in load marking Stage III is
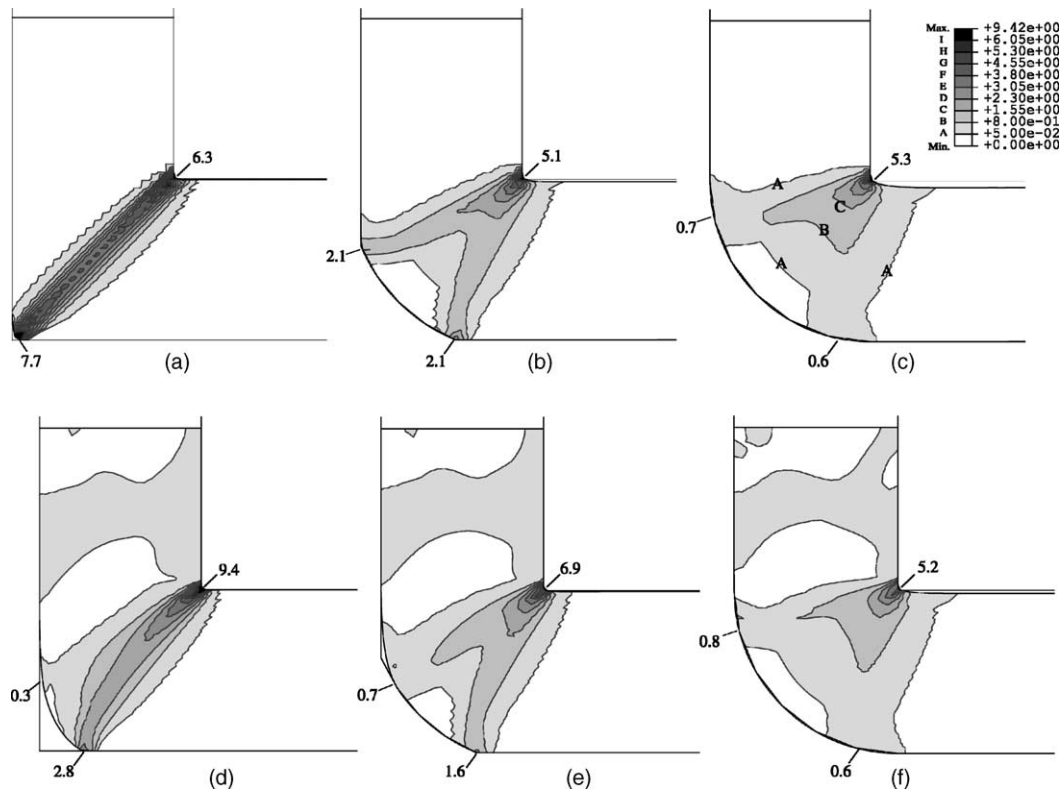
Fig. 17. Influence of friction coefficient μ on the distribution of equivalent plastic strain-rates (s^{-1}) within the PDZ (a–c) cases 7–9 and (d–f) cases 10–12, respectively.

associated with the abrupt increase of deformation in the billet head. The load decreases gradually with the displacement in Stage IV, and then remains constant in Stage V until the end of the ECAE. As can be seen from the comparison of Fig. 21c and d, the decrease of load in Stage IV is associated with the decrease of plastic deformation in the billet head. The transient point from Stage IV to Stage V (Fig. 21d) is the moment when the non-uniformly deformed billet head completely moves out of the deformation zone in the die corner. Note that there is a sudden drop of load at a ram displacement of $\sim 5.2w$ in Stage V. This is due to the loss of contact between the upper surface of the billet head and the outlet channel when the billet head comes out of the outlet channel (see Fig. 21e) and thus depends on the length of the outlet channel. Characteristics in the first three stages for $\Psi > 0°$ coincide with those identified by Kim [26] in an FE simulation carried out for $\Phi = 90°$ and $\Psi = 90°$ and for a strain hardening 1100 Al alloy under frictionless conditions.

The stages in the load–displacement curves for the SH material are more pronounced than for the PP material (Fig. 19a). In general, in the latter, the transient Stage II and Stage III for $\Psi = 0°$ and Stage IV for $\Psi > 0°$ do not occur. This suggests that these stages manifested in the SH material due to the more complex variation in strain-rate across the billet. The remaining stages are dependent on the deformation in the billet head, which in turn, is influenced by Ψ, strain hardening and friction conditions.

Apart from increasing the overall load, friction changes the final steady-state stage, from a plateau for $\mu = 0$ to a steady decline for $\mu > 0$ (see Figs. 18b and 19b). The decrease of load in the steady state is related to the dependence of frictional forces on gap formation in the outlet. In general, the billet is in full contact with the die wall in the inlet channel, but only partially in contact with the wall in the outlet due to the formation of gaps. When the billet is pressed from the inlet channel to the outlet channel through the die corner, the contact area in the inlet channel decreases and in the meantime the length of the gap in the outlet channel grows until the head of the billet comes out of the outlet channel. As a result, the total contacting area between the billet and the die wall always decreases with the ram displacement, and so when $\mu > 0$, the response is visible in the load versus displacement curve.

The magnitude of the maximum load is most interesting from the viewpoint of die designs. The present results show that for $\Psi = 0°$, the peak load is reached prior to achieving steady state and is substantially higher than the steady state load for the SH material, whereas the load in the steady state is equal or close to the peak load for the PP material. In the same material, the peak load decreases with Ψ and increases with μ.
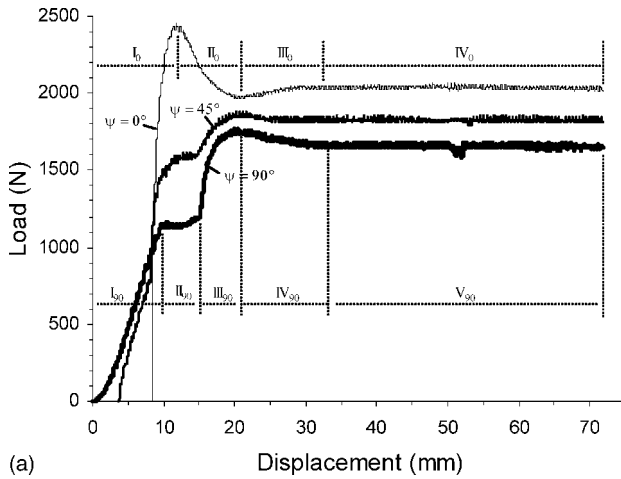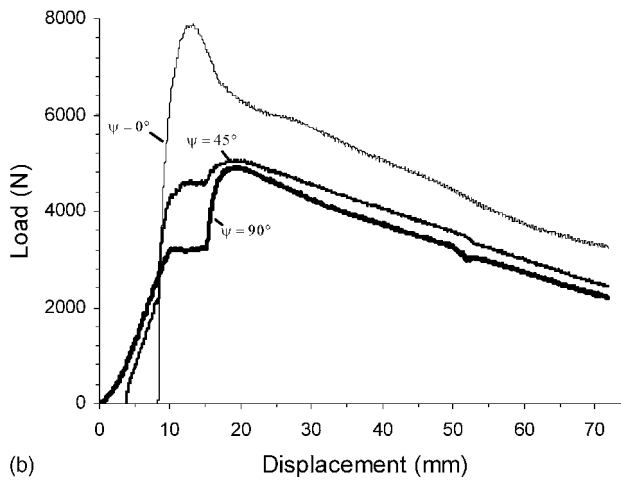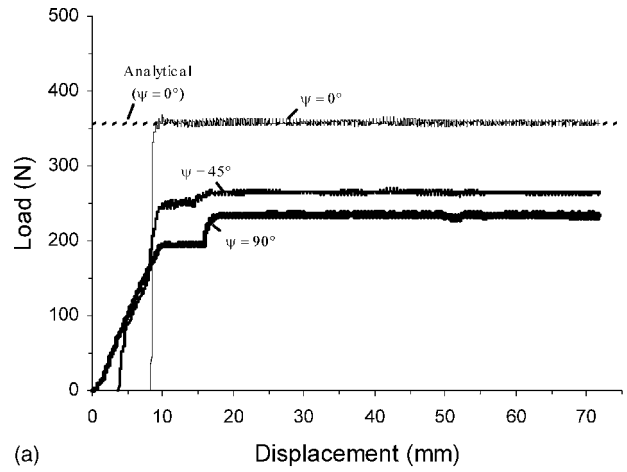
Fig. 18. Influence of Ψ on the working load–ram displacement curves simulated for a strain hardening material for (a) $\mu = 0$ and (b) $\mu = 0.075$.

Fig. 19. Influence of Ψ on the working load–ram displacement curves simulated for a perfectly plastic material for (a) $\mu = 0$ and (b) $\mu = 0.025$. The analytical result for the case of $\Psi = 0°$ shown in panel (a) was calculated from Eq. (7).
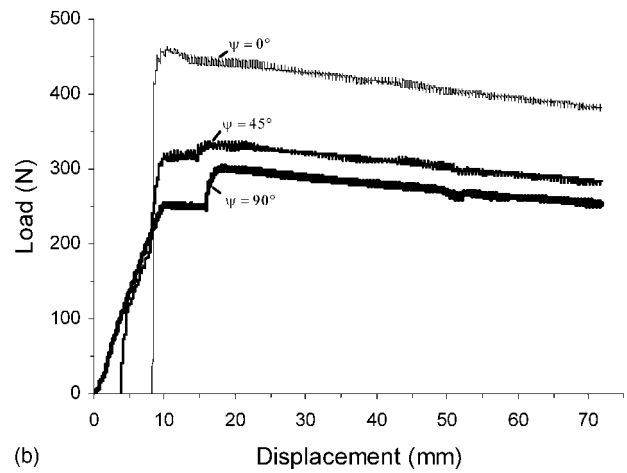
4. Summary

FE simulations of the ECAE process were carried out for a perfectly plastic (PP) and a strain hardening (SH) material using a die with an intersection angle of 90°. The effects of the outer corner angle Ψ, strain hardening, and friction on the overall deformation behavior, PDZ, and working load were evaluated.

Regarding the overall deformation behavior, the following conclusions can be drawn from the results:

(1) The head and tail of the billet undergo non-uniform deformation during a single pass of ECAE. Minimizing the lengths of these non-uniform regions is of interest for maximizing the length of the useful homogeneous portion of the billet. For the same Ψ, the non-uniformly deformed head part is longer in the SH material than in the PP material. With the increase of Ψ, the length of this part increases appreciably in the PP material but remains almost constant in the SH material.

(2) In the steady-state region, significant strain inhomogeneity exists across the billet width (e.g. top to bottom) for all cases except for the PP material with $\Psi = 0°$; it also increases with Ψ in both materials, although this effect is less significant in the SH material. It also increases with friction in most cases.

(3) Due to inhomogeneous deformation induced by strain hardening, rounded corner dies $\Psi > 0°$, and friction, gaps can develop both in the outer die corner and in the outlet channel. Specifically the size of the corner gap decreases with Ψ and increases with the hardening rate. In contrast, the size of the outlet channel gap as a result of billet bending, increases with Ψ and decreases with the hardening rate. Both the corner gap and the channel gap decrease with friction.

The above conclusions on the heterogeneity in the final deformation can be explained through changes in two chief characteristics of the PDZ, its shape and its strain-rate distribution. In this work, both yield indicator and strain-rate distribution plots were compared among the different combinations of Ψ, μ, and material response. The following conclusions can be drawn from these results.
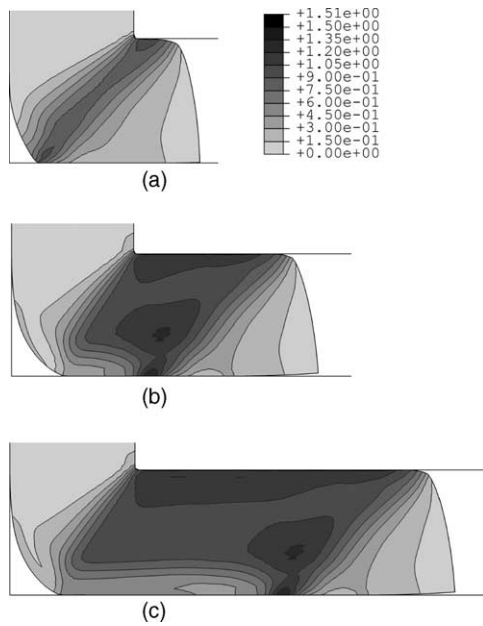
Fig. 20. Evolution of the equivalent plastic strain distribution in the billet at a ram displacement of (a) 1.3w (transition between Stage I and Stage II), (b) 2.2w (transition between Stage II and Stage III), and (c) 3.2w (transition between Stage III and Stage IV) for case 4 [SH, $\Psi = 0°$, $\mu = 0$].

(1) Under frictionless conditions, for the PP material with $\Psi = 0°$, the PDZ is confined in a narrow region around the intersection plane. In all other cases the PDZ essentially consists of three regions due to the outer curvature of the die $\Psi > 0°$ or to a free surface corner gap or both.

(2) The largest region is a fan around the inner corner and the other two regions are generally located around the outer corner either where the material separates from the die in cases of a corner gap, or otherwise, where the inlet and outlet channels intersect the rounded corner. The central fan is where most of the intense severe plastic deformation occurs and the last two regions are nearly equivalent regions of localized plastic deformation bounding a region of rigidly rotating material centered between them.

(3) The size of the PDZ, β, was estimated for each case by fitting the FE effective strains with a prediction of the effective strain based on a fan-shaped PDZ. The inner angle β of the PDZ was found to increase with Ψ and with corner gap size and to be comparable to those observed in FE calculations. In general, these two angles, Ψ and β, are not equal.

(4) As material strain hardening increased, the distribution of strain-rates within the PDZ became asymmetric.

(5) We introduced the concept of a maximum applicable friction coefficient, μ_m, below which a steady-state region develops in the billet after successful completion of the ECAE simulation. FE calculations above this
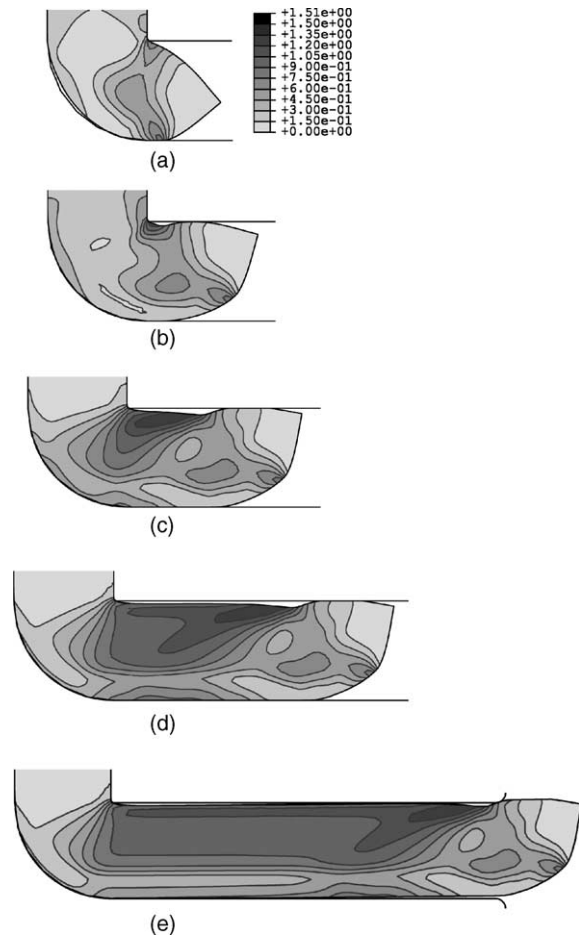

Fig. 21. Evolution of the equivalent plastic strain distribution in the billet at a ram displacement of (a) 1.1w (transition between Stage I and Stage II), (b) 1.5w (transition between Stage II and Stage III), (c) 2.1w (transition between Stage III and Stage IV), (d) 3.2w (transition between Stage III and Stage IV), and (e) 5.2w (drop of load in Stage V), for case 6 [SH, $\Psi = 90°$, $\mu = 0$].

value are likely not to be accurate or useful. μ_m increases as the length of the billet or the exit channel is reduced.

(6) We introduced an inhomogeneity index, C_i, based on the spatial variation of plastic strain within the steady-state region and found that it generally increases with Ψ, strain hardening, and friction coefficient μ, if no corner gap is formed.

(7) Within the investigated range of friction coefficients $\mu < \mu_m$, friction was found to have little effect on the shape of the PDZ when the material fills the die. However, it had some effect on the local variation of strain-rates at the inner and outer corner regions. Specifically an increase of friction leads to a higher plastic strain-rate in the inner corner and variation of the strain-rates near the outer corner region. Therefore a higher degree of inhomogeneity, i.e. higher C_i, results from friction, even when the material fills the die, which is contrary to popular belief.

The stages that manifest in the working load versus ram displacement curve are studied for all cases shown in Table 1. From these results, we can conclude the following.

(1) The variation of load with displacement before the process enters steady state is dependent on the deformation in the billet head, which in turn, is influenced by the outer corner angle, strain hardening and friction conditions.

(2) These curves are more complex in the SH material than in the PP material. Under the frictionless conditions, the maximum load is higher than the load in the steady-state stage in the SH material, whereas in the PP material the load in steady state is also the maximum load in the whole process.

(3) For the same material, the maximum load in ECAE decreases with Ψ and increases with friction.

(4) The ram displacement for which the deformation enters steady state depends on the deformation in the billet head, which in turn, is influenced by Ψ, strain hardening and friction conditions. The evolution of load associated with steady state depends on the friction coefficient and filling status in the outlet channel. When friction exists, the steady-state load decreases with the displacement when outlet channel gaps form. When it does not, the steady-state load is constant.

To date, most of the cases studied here have not been modeled analytically; however, a stronger connection between analytical modeling and actual ECAE deformation can be made by the guidance of these FE studies on the interactive influence of processing and material variables on the PDZ and working load.

Acknowledgements

References

[1] V.M. Segal, V.I. Reznikov, A.E. Drobyshevkiy, V.I. Kopylov, Russ. Metall. 1 (1981) 99.
[2] V.M. Segal, Mater. Sci. Eng. A 197 (1995) 157.
[3] R.Z. Valiev, R.K. Islamgaliev, I.V. Alexandrov, Prog. Mater. Sci. 45 (2000) 103.
[4] V.M. Segal, Mater. Sci. Eng. A 271 (1999) 322.
[5] V.M. Segal, Mater. Sci. Eng. A 345 (2003) 36.
[6] Y. Iwahashi, J. Wang, Z. Horita, M. Nemoto, T.G. Langdon, Scr. Mater. 35 (1996) 143.
[7] G.M. Stoica, P.K. Liaw, JOM 53 (2001) 36.
[8] D.N. Lee, Scr. Mater. 43 (2000) 115.
[9] I.J. Beyerlein, C.N. Tomé, Analytical modeling of material flow in equal channel angular extrusion. Mater. Sci. Eng. A 380 (2004) 171–190.
[10] I.J. Beyerlein, S. Li, D.J. Alexander, C.T. Necker, C.N. Tomé, M.A.M. Bourke, in: Y.T. Zhu, T.G. Langdon, R.Z. Valiev, S.L. Semiatin, D.H. Shin, T.C. Lowe (Eds.), Ultrafine Grained Materials III, TMS (The Minerals, Metals & Materials Society), Charlotte, NC, 2004, p. 185.
[11] S.L. Semiatin, D.P. Delo, E.B. Shell, Acta Mater. 48 (2000) 1841.
[12] H.S. Kim, M.H. Seo, S.I. Hong, Mater. Sci. Eng. A 291 (2000) 86.
[13] H.S. Kim, S.I. Hong, M.H. Seo, J. Mater. Res. 16 (2001) 856.
[14] B.S. Moon, H.S. Kim, S.I. Hong, Scr. Mater. 46 (2002) 131.
[15] J.R. Bowen, A. Gholinia, S.M. Roberts, P.B. Prangnell, Mater. Sci. Eng. A 287 (2000) 87.
[16] R. Srinivasan, Scr. Mater. 44 (2001) 91.
[17] J.-Y. Suh, H.-S. Kim, J.-W. Park, J.-Y. Chang, Scr. Mater. 44 (2001) 677.
[18] J.-W. Park, J.-Y. Suh, Metall. Mater. Trans. 32A (2001) 3007.
[19] H.S. Kim, J. Mater. Res. 17 (2002) 172.
[20] H.S. Kim, M.H. Seo, S.I. Hong, J. Mater. Process. Technol. 113 (2001) 622.
[21] D.P. Delo, S.L. Semiatin, Metall. Mater. Trans. 30A (1999) 1391.
[22] P.B. Prangnell, C. Harris, S.M. Roberts, Scr. Mater. 37 (1997) 983.
[23] V.S. Zhernakov, I.N. Budilov, G.I. Raab, I.V. Alexandrov, R.Z. Valiev, Scr. Mater. 44 (2001) 1765.
[24] S.J. Oh, S.B. Kang, Mater. Sci. Eng. A 343 (2003) 107.
[25] L. Zuyan, W. Zhongjin, J. Mater. Process. Technol. 94 (1999) 193.
[26] H.S. Kim, Mater. Sci. Eng. A 315 (2001) 122.
[27] H.S. Kim, Mater. Sci. Eng. A 328 (2002) 317.
[28] ABAQUS User's Manual, Version 6.3, Hibbitt, Karlsson & Sorensen, Inc., 2002.